

Corrosion and Algal Adhesion Behaviors of HVOF-Sprayed Fe-Based Amorphous Coatings for Marine Applications

Haijun Zhang^{1,2} · Yongfeng Gong² · Botao Zhang³ · Xiuyong Chen² · Lijia Fang^{1,2} · Peipeng Jin¹ · Hua Li²

Submitted: 5 April 2018 / in revised form: 21 August 2018 / Published online: 22 October 2018
© ASM International 2018

Abstract In this study, Fe-based amorphous/nanocrystalline coatings consisting of $\text{Fe}_{53}\text{Cr}_{19}\text{Zr}_7\text{Mo}_2\text{C}_{18}\text{Si}$ were fabricated by high-velocity oxy-fuel spray. For comparative study, further crystallization annealing treatment at 750 °C was carried out for the coatings. The microstructure, corrosion resistance and algal adhesion behaviors of the as-sprayed and annealed coatings were systematically investigated by scanning electron microscopy, x-ray diffraction, transmission electron microscopy, electrochemical testing and laser confocal scanning microscopy, respectively. Results show that the as-sprayed coatings exhibited excellent corrosion resistance and decreased

algal adhesion, while the annealed coatings displayed compromised anti-corrosion performances, but significantly inhibited the adhesion of typical algae *Phaeodactylum tricorutum*.

Keywords algal adhesion · corrosion resistance · Fe-based amorphous coating · high-velocity oxy-fuel · marine coatings · nanocrystalline

Introduction

Biofouling and corrosion are the two major problems for marine equipment (Ref 1, 2). To date, varieties of techniques have been explored to alleviate or prevent the occurrence of corrosion (Ref 3, 4) and biofouling (Ref 5–9) in marine environment, among which thermal-sprayed metallic coatings have shown long-term protection for marine artificial infrastructures (Ref 10, 11). For example, thermal-sprayed metallic coatings (Fe-based amorphous coating and Al-based marine coatings) (Ref 12, 13) and polyethylene–Cu composite coatings (Ref 10) have been proven to perform well in simulated marine environment. Our recent researches showed that thermal-sprayed superhydrophobic and micropatterned surfaces displayed excellent anti-corrosion and anti-biofouling performances (Ref 9, 14). However, knowledge about corrosion and biofouling behaviors of thermal-sprayed coatings in the marine environment is still insufficient.

Thermal-sprayed Fe-based amorphous/nanocrystalline coatings have attracted much attention for potential applications, owing to their excellent anti-corrosion/wear performances, high strength, low material cost and processing capabilities. Thermal spray processing such as atmospheric plasma spray (Ref 15), arc spray (Ref 16), kinetic spray

This article is an invited paper selected from presentations at the 2018 International Thermal Spray Conference held on May 7–10, 2018 in Orlando, Florida, USA, and has been expanded from the original presentation.

✉ Xiuyong Chen
chenxiuyong@nimte.ac.cn

✉ Peipeng Jin
peipeng.jin@qhu.edu.cn

✉ Hua Li
lihua@nimte.ac.cn

¹ Qinghai Provincial Key Laboratory of New Light Alloys, Qinghai Provincial Engineering Research Center of High Performance Light Metal Alloys and Forming, Qinghai University, Xining 810016, People's Republic of China

² Key Laboratory of Marine Materials and Related Technologies, Zhejiang Key Laboratory of Marine Materials and Protective Technologies, Ningbo Institute of Materials Technology and Engineering, Chinese Academy of Sciences, Ningbo 315201, People's Republic of China

³ Cixi Institute of Biomedical Engineering, Institute of Materials Technology and Engineering, Chinese Academy of Sciences, Ningbo 315201, People's Republic of China

(Ref 17) and high-velocity oxy-fuel (HVOF) spray (Ref 18) has been successfully used for fabricating Fe-based coatings with hybrid amorphous/nanocrystalline structures. Among the abovementioned thermal-sprayed coatings, HVOF-sprayed coatings have favorable properties such as lower porosity, higher adhesion, higher hardness and compression stresses (Ref 19, 20). Furthermore, many studies have implied that thermal-sprayed Fe-based amorphous coatings exhibit excellent corrosion resistance (Ref 21, 22). For instance, Farmer et al. have demonstrated that thermal-sprayed $\text{Fe}_{49.7}\text{Cr}_{17.7}\text{Mn}_{1.9}\text{W}_{1.6}\text{B}_{15.2}\text{C}_{3.8}\text{Si}_{2.4}$ (SAM2X5) coatings with amorphous structure can provide outstanding corrosion resistance in chloride solution (Ref 21). Zhang et al. prepared an $\text{Fe}_{48}\text{Cr}_{15}\text{Mo}_{14}\text{C}_{15}\text{B}_6\text{Y}_2$ amorphous coating by HVOF method, and the corrosion behavior of the coatings was investigated in 3.5 wt.% NaCl solution (Ref 23). Mahata et al. reported the electrochemical behavior of $\text{Fe}_{73.13}\text{Si}_{11.12}\text{B}_{10.79}\text{Cr}_{2.24}\text{C}_{2.72}$ coating with amorphous/nanocrystalline hybrid structures, and the coating showed excellent corrosion resistance (Ref 24). Our earlier study has demonstrated that the microstructure, corrosion resistance and cell adhesion were significantly affected by additional annealing treatment of the Fe-based amorphous coatings (Ref 11). Nevertheless, to the best of our knowledge, this is the first study on adhesion of typical microfoulers on thermal-sprayed Fe-based amorphous/nanocrystalline coatings.

In this study, Fe-based amorphous/nanocrystalline composite coatings were deposited on 316L stainless steel (316L SS) substrates by HVOF spraying. Crystallization of the as-sprayed coatings was accomplished by further annealing treatment. To comparatively investigate the influence of amorphicity of the coatings on microstructure, corrosion resistance and algal adhesion behaviors of the coatings, both the as-sprayed and annealed coatings were investigated.

Materials and Methods

Micron-sized (+ 30–150 μm) Fe-based powder with an amorphicity of 36.82% made by gas atomization in high-pressure argon atmosphere was used as the starting feedstock. Fe-based amorphous/nanocrystalline coatings consisting of $\text{Fe}_{53}\text{Cr}_{19}\text{Zr}_7\text{Mo}_2\text{C}_{18}\text{Si}$ with an enhanced amorphicity of 55.85% were prepared by a HVOF system (CJK5, Castolin Eutectic, Germany) (Ref 11). The spraying parameters employed in the HVOF process are presented in Table 1. 316L SS plates with a dimension of $20 \times 20 \times 2$ mm were used as substrates. Prior to the deposition, the substrates were degreased in acetone, dried in air and sandblasted. For further crystallization treatment, the as-sprayed coatings were heat-treated at 750 °C (based

Table 1 HVOF spray parameters

Oxygen flow rate, mL/min	800 mL/min
Kerosene flow rate, mL/min	400 mL/min
Spraying distance, mm	300 mm
Carrier gas flow rate, mL/min	8.5 mL/min
Feed rate, g/min	35 g/min

on the DSC analysis) for 1 h and then naturally cooled down to room temperature in a vacuum furnace (Ref 11).

Microstructure of the feedstock powder and the coatings was examined by field emission scanning electron microscopy (FESEM) (FEI Quanta FEG250, the Netherlands) equipped with energy-dispersive spectroscopy (EDS). Selected area electron diffraction (SEAD) and the coatings' finer-scale microstructure characterization were performed by transmission electron microscopy (TEM, FEI Tecnai F20, the Netherlands). Phase composition of the samples were investigated by x-ray diffraction (XRD, D8 Advance, Bruker AXS, Germany) with Cu $K\alpha$ radiation operated at 40 kV and a scanning rate of 0.1°/s. The goniometer was run with a step size of 0.033°/s from 20° to 90° of 2θ . XRD patterns were used to calculate the amorphicity of the powder, the as-sprayed coatings and the annealed coatings.

Prior to potentiodynamic polarization testing, the samples were mirror-polished and then degreased with acetone, ultrasonically washed with deionized water and dried, respectively. All the samples were sealed by epoxy to gain an exposed testing surface area of 10×10 mm² and immersed in 3.5 wt.% NaCl solution for 1 h before electrochemical signals were acquired. Each testing was repeated at least three times to ensure reproducibility. A traditional three-electrode cell was used, with a platinum plate as the counter-electrode, the specimen having an exposed area of 10×10 mm² as the working electrode and a saturated calomel electrode (SCE) as the reference electrode. Potentiodynamic polarization of the samples was assessed in 3.5 wt.% NaCl solution at room temperature using a Solartron Modulab System (2100A, UK). Potentiodynamic polarization curves were obtained with a potential scan rate of 0.5 mV/s. The surfaces of the samples after potentiodynamic polarization testing were observed by SEM.

Phaeodactylum tricorutum was used as the model organism in this study (Ref 25, 26). Artificial seawater (ASW) was prepared according to ASTM D1141-98. *Phaeodactylum tricorutum* was cultured in silicate-enriched Guillard's F/2 growth medium at 20 °C. Algae during exponential phase growth were used for the testing. The samples were firstly polished to mirror finish and then ultrasonically cleaned with ethanol and deionized water,

respectively. Subsequently, the samples were dried in air at 37 °C and sealed by epoxy to obtain an exposed area of $10 \times 10 \text{ mm}^2$. Finally, they were vertically put into beakers containing *Phaeodactylum tricornutum* and cultured for 1, 3 and 7 days, respectively, in a growth chamber with a 12 h:12 h light/dark cycle at 22 °C. Each beaker contained 120 mL algal suspension with an initial algal concentration of $5 \times 10^6 \text{ mL}^{-1}$. After incubation, the samples were washed with sterile ASW for three times to remove non-adhered algae, fixed by 2.5% glutaraldehyde for 2 h and then examined by confocal laser scanning microscopy (CLSM, Leica TCS SP5, Germany) and FESEM. The adhesion ratios were quantified by using the software image. The statistical analysis was performed at confidence levels of 95% and 99% by one-sample test (OriginPro version 8.5).

Results and Discussion

The morphology of the powder feedstock is shown in Fig. 1. Majority of the particles are spherical with the diameters of $\sim 30\text{--}150 \mu\text{m}$ (Fig. 1). XRD patterns of the powder and coatings are shown in Fig. 2. The XRD pattern of the as-sprayed coating exhibited a broad halo peak around $2\theta \approx 45^\circ$, indicating the predominate presence of amorphous phase in the as-sprayed coating. It is noted that the powder shows several crystalline diffraction peaks, suggesting certain nanocrystalline phases. The major crystalline phase is found to be composed of $\alpha\text{-Fe}$ (JCPDS Card No.: 65-4899). The as-sprayed coating only shows a broader and weaker halo peak, indicating enhanced amorphicity as compared to the starting feedstock. This phenomenon can be explained that HVOF deposition processing brings about high cooling rate for sprayed droplets upon impingement onto substrate surface (Ref 27).

On the contrary, after annealing treatment of the as-sprayed coating for 1 h at 750 °C, the broad halo peak almost disappears and sharper crystalline peaks emerge, indicating formation of nanocrystalline phases ($\alpha\text{-Fe}$) (Ref 11, 18). This is likely owing to recrystallization of the amorphous phase.

Characterization of the surface and the cross-sectional morphology of the as-sprayed and annealed coatings shows well-flattened splats and partially melted particles in the coatings (Fig. 3). The presence of the heterogeneous phases suggests that some particles were not fully melted during the spraying process (Fig. 3a-1). The as-sprayed coating exhibits a thickness of $\sim 150 \mu\text{m}$ (Fig. 3a-3). In addition, some visible pores were observed from the cross section of the as-sprayed coating. After the annealing treatment, weakened splats' interfaces but densified structures with diminished flaws can be seen in Fig. 3(b-3). A

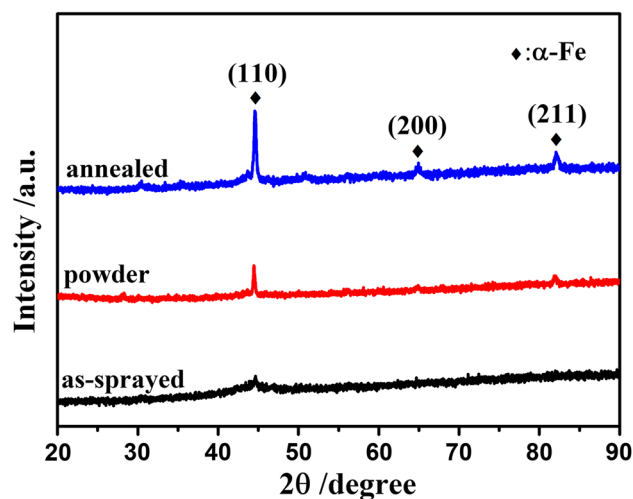


Fig. 2 XRD patterns of the powder, the as-sprayed coating and the annealed coating

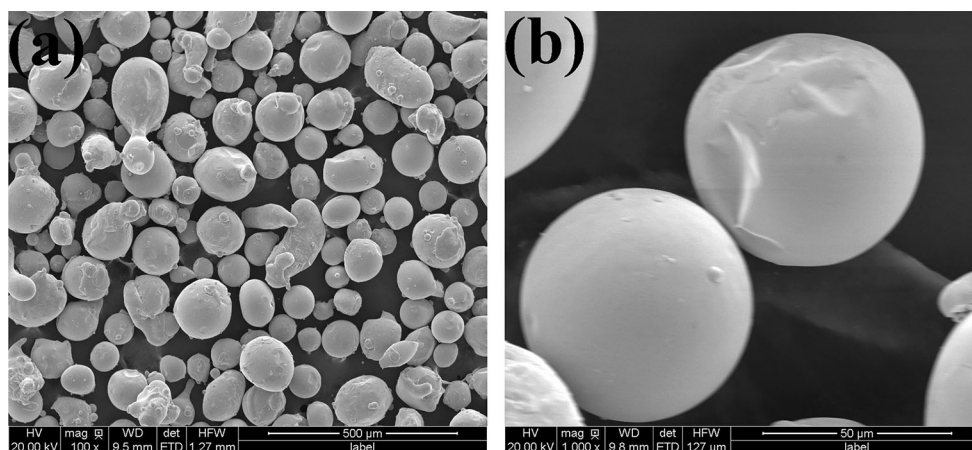


Fig. 1 FESEM images of the starting powder (b) is enlarged views of selected particles shown in (a)

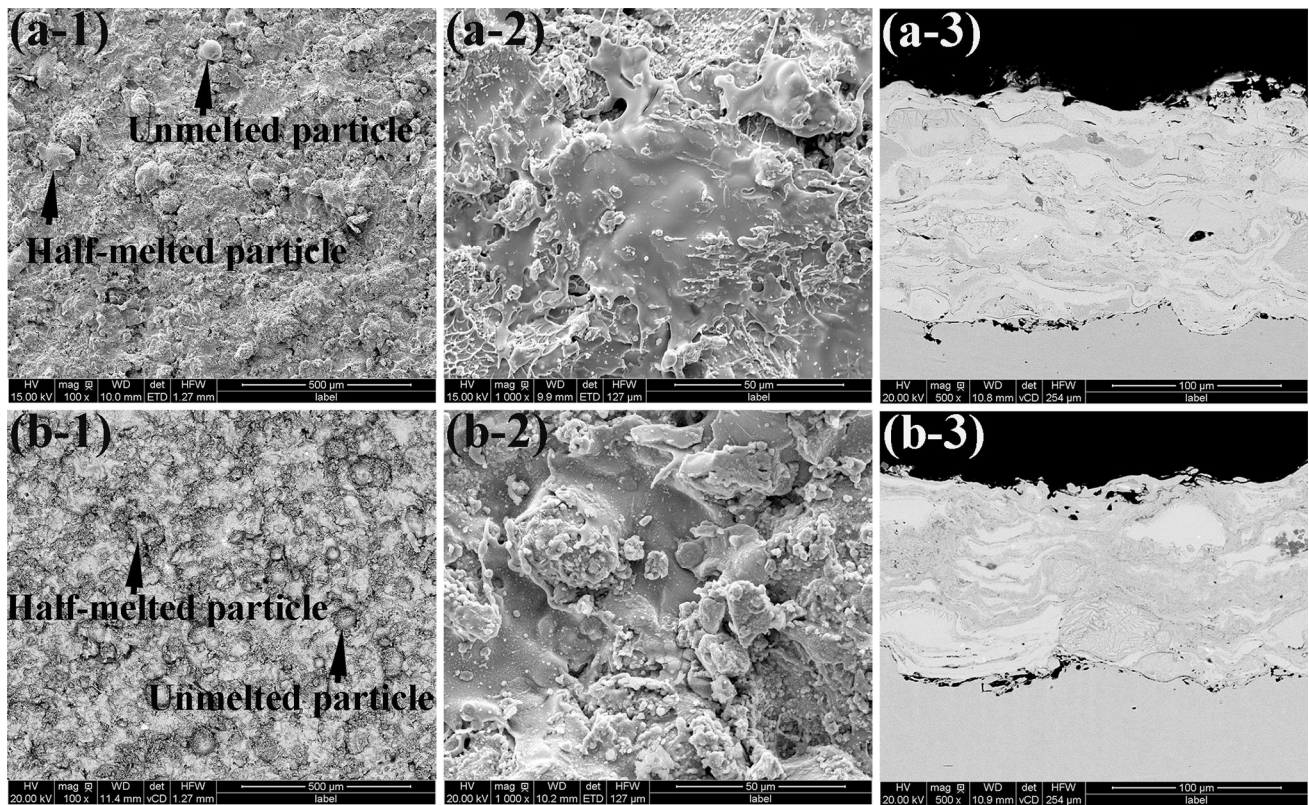


Fig. 3 FESEM images showing the topographical and cross-sectional morphologies of the as-sprayed coating (a) and the annealed coating (b) (– 2 are enlarged views of selected area in – 1, scale bar: 500 μm in (a-1, b-1), 50 μm in (a-2, b-2), 100 μm in (a-3, b-3), respectively)

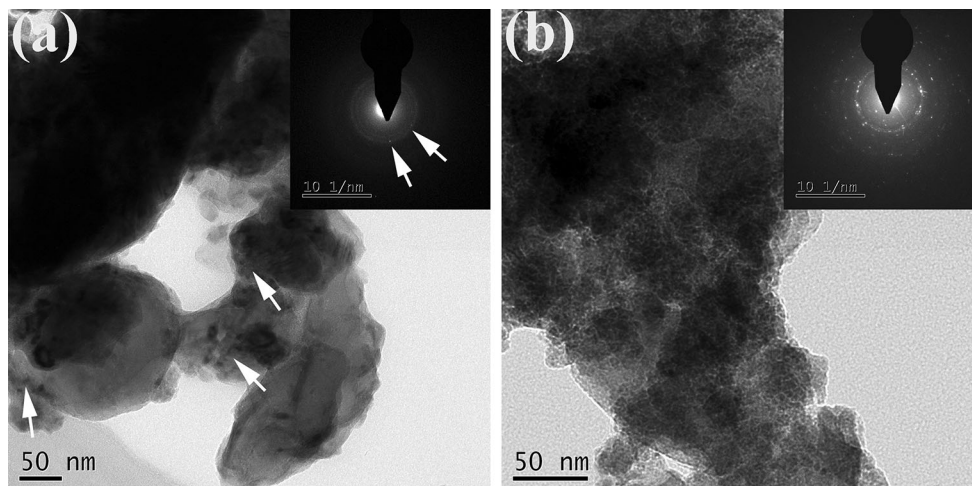


Fig. 4 TEM images of the as-sprayed coating (a) and the annealed coating (b)

similar phenomenon has been reported, which might be due to possible occurrence of diffusion and sintering during heat treatment process (Ref 11).

To further investigate the microstructure of the coatings, TEM characterization was carried out (Fig. 4). It can be seen from the selected area electron diffraction (SAED) pattern (inset of Fig. 4a) that few spots are superimposed on the diffused halo ring and some nanocrystalline grains

can be observed in the corresponding bright field (highlighted by the arrowhead, Fig. 4a), indicating that the majority of the phases in the as-sprayed coating are amorphous and a small fraction of nanocrystalline phase is not uniformly embedded in the amorphous matrix. However, the SAED pattern (inset of Fig. 4b) shows much more nanocrystalline phases in the annealed coating than those in the as-sprayed coating. Also amorphous and

nanocrystalline phases can be clearly seen in the bright field (Fig. 4b). It is likely that crystallization of the amorphous matrix results in formation of nanocrystalline grains

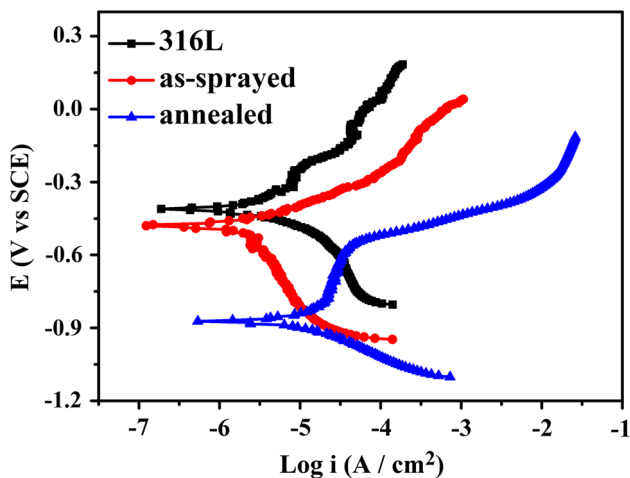
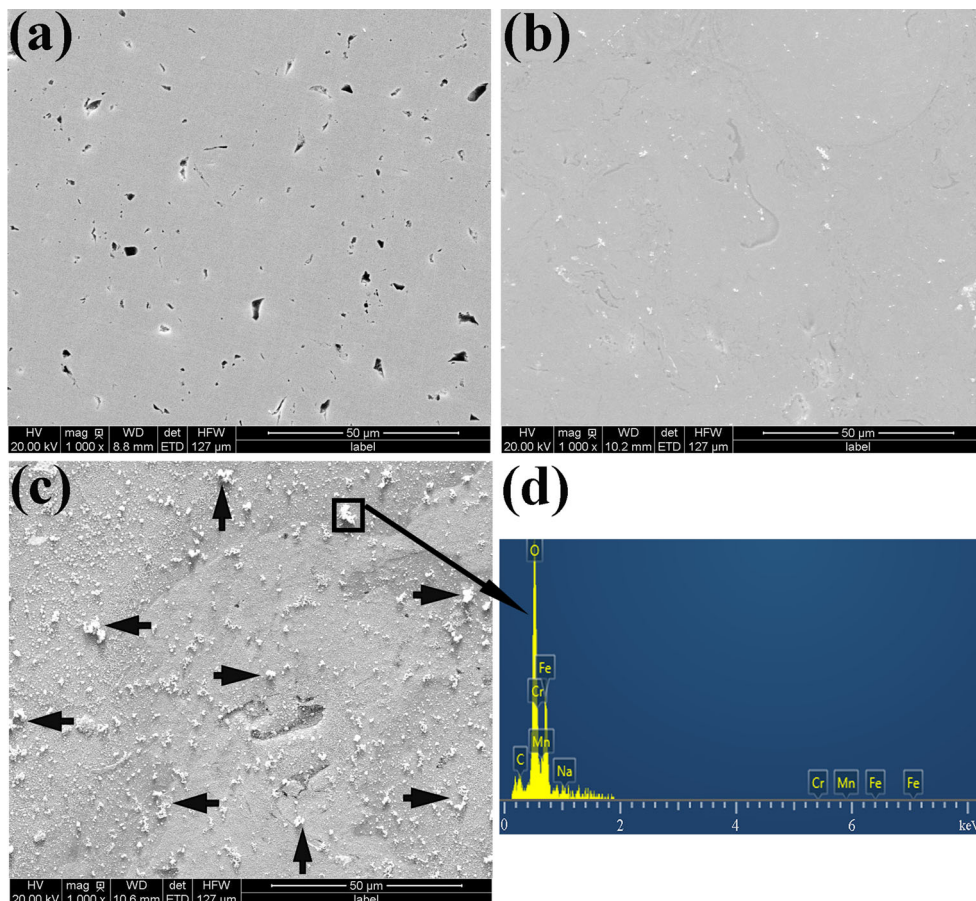


Fig. 5 Potentiodynamic polarization curves of the 316L SS, the as-sprayed coating and the annealed coating tested in 3.5% NaCl solution

in the annealed coatings. This is consistent with the XRD result (Fig. 2).

The coatings exhibit a hybrid structure of amorphous and nanocrystalline phases with the composition of $Fe_{53}Cr_{19}Zr_7Mo_2C_{18}Si$. It is known that the addition of Mo and Cr can enhance the corrosion resistance of the Fe-based amorphous/nanocrystalline composite coatings (Ref 28). Cr is one of the key passivating elements for high corrosion resistance, while Mo can prevent the dissolution of Cr during passivation to stabilize the passive film. Figure 5 shows the potentiodynamic polarization curves of the 316L SS, the as-sprayed coating and the annealed coating tested in 3.5 wt.% NaCl solution. The corrosion current density of the as-sprayed coating ($7.856 \times 10^{-7} A/cm^2$) is much lower than that of the annealed coating ($5.304 \times 10^{-6} A/cm^2$). It is believed that a lower corrosion current density corresponds to a lower corrosion rate (Ref 29, 30). It is likely that the ultrafine nanocrystalline phases uniformly embedded in the amorphous matrix provide homogenous substrate for formation of passive film to improve the corrosion resistance. In contrast, the annealed coating displays lower corrosion potential (E_{corr}) and higher passive current density (I_{corr}) than the 316L SS and the as-sprayed coating, suggesting deteriorated corrosion resistance. This

Fig. 6 FESEM micrographs of (a) the 316L SS, (b) the as-sprayed coating and (c) the annealed coating after the polarization test in 3.5 wt.% NaCl solution (scale bar: 50 μm) and (d) EDS spectra of the corrosion products formed on the annealed coating



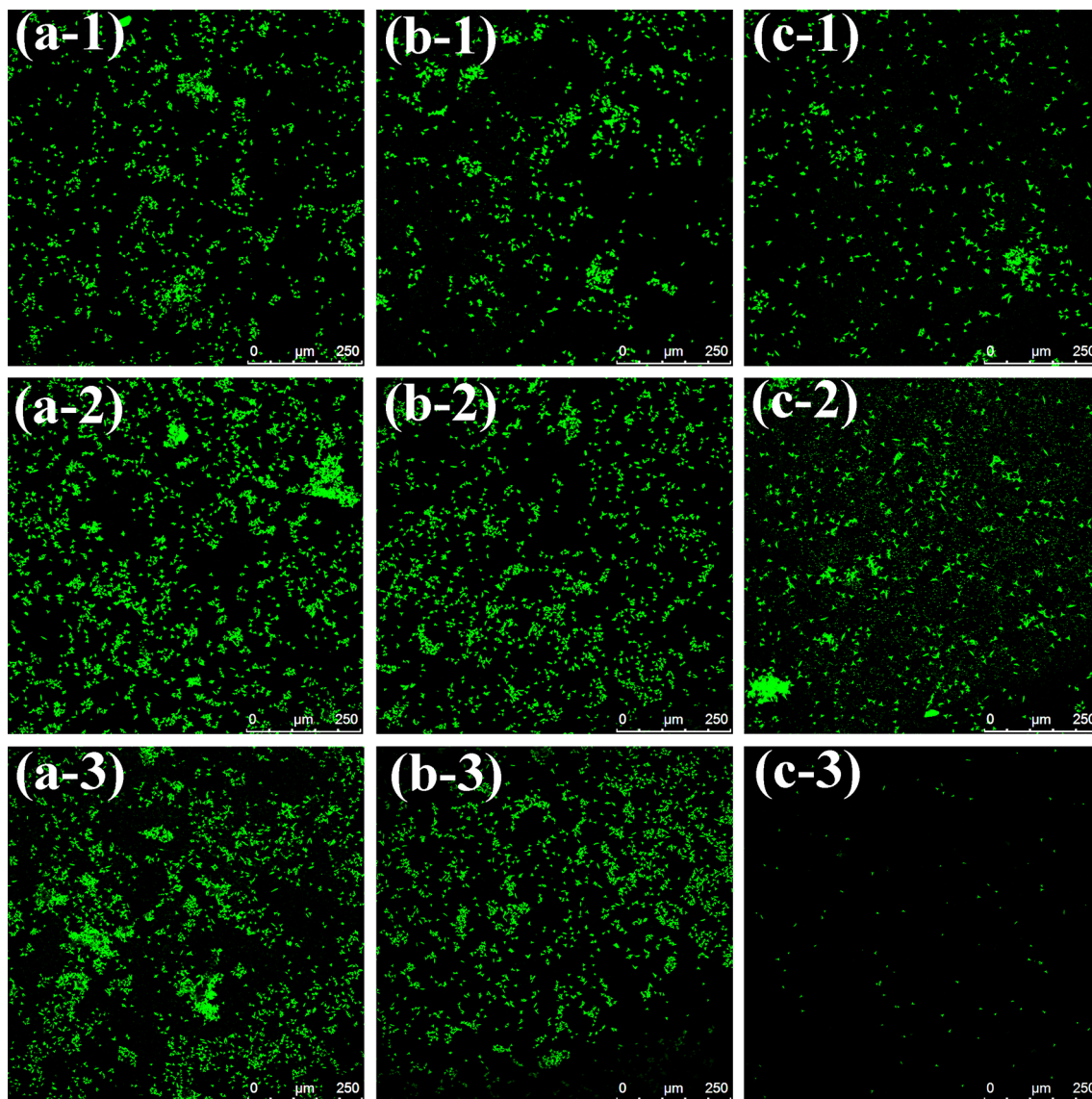


Fig. 7 CLSM images showing the adhesion of *Phaeodactylum tricorutum* on (a) the 316L SS, (b) the as-sprayed coating and (c) the annealed coating after incubation in *Phaeodactylum*

tricorutum-containing solution (– 1 is for 1 day, – 2 is for 3 days, – 3 is for 7 days, scale bar: 250 μm)

is probably due to the combining effect brought about by crystallization treatment and porosity. It has been reported that crystallization treatments could generate grain boundaries, crystalline defects and segregates (Ref 31). In addition, the annealed coating can passivate spontaneously with the lowest pitting potential, implying a relatively lower pitting corrosion resistance than those of the 316L SS and the as-sprayed coating.

Furthermore, obvious pits can be observed on the 316L SS plate after the polarization testing (Fig. 6a). On the contrary, fewer and smaller pits are sparsely distributed on the surface of the as-sprayed coating (Fig. 6b), indicating its better corrosion resistance property. This might mainly result from its homogeneous phase structure. However, for

the annealed coating, the corrosion damage became more serious as indicated by numerous corrosion products (Fig. 6c). Cr-related or Fe-related corrosion products formed on the surfaces of the annealed coatings, likely leading to breakdown of the passivity. In addition, metal oxides can impede formation of dense passive films and even become the diffusion channels for electrolyte in sodium chloride solution and consequently cause inner corrosion (Ref 27). Corrosion damages mainly occur at intersplats where oxygen is enriched (Ref 32) and crystallization initiated. And formation of carbides simultaneously affects structures and compositions of passive film, decreasing productivity of passive film through reducing

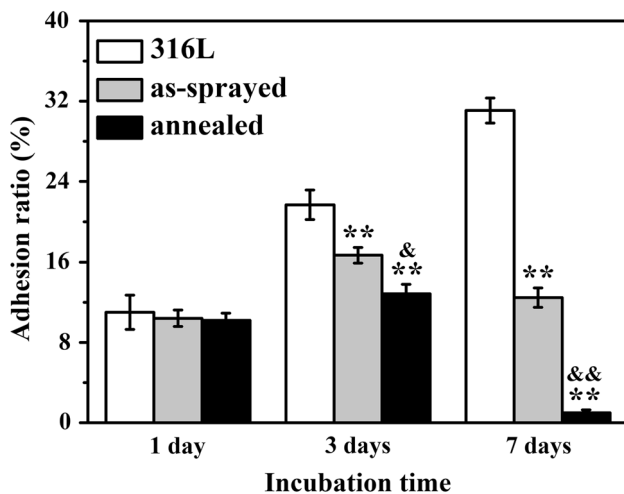


Fig. 8 Adhesion ratio of *Phaeodactylum tricorutum* on the samples (area %). Error bars are shown as \pm SD ($n = 3$). * $p < 0.05$ and ** $p < 0.01$ compared with the 316L SS, & $p < 0.05$ and && $p < 0.01$ compared with the as-sprayed coating

the amount of (Cr, Mo) oxides. This phenomenon agrees well with our electrochemical testing result (Fig. 5).

Figure 7 shows CLSM observation of the adhesion of typical algae *Phaeodactylum tricorutum* on the 316L SS, the as-sprayed coatings and the annealed coatings. After incubation for 1 day, comparable algal adhesion on the surfaces of the 316L SS, the as-sprayed coatings and the annealed coatings is seen (Fig. 7-1). After incubation for 3 days, the amount of the adhered alga sharply increased on all the samples, yet fewer alga adhered on the as-sprayed coatings and the annealed coatings than that on the 316L SS (Fig. 7-2). As incubation time was prolonged to 7 days, further enhanced adhesion of *Phaeodactylum tricorutum* is seen on the surface of the 316L SS (Fig. 7-3). However, it is worth noting that the adhesion of *Phaeodactylum tricorutum* on the coatings, especially on the annealed coatings, was significantly inhibited (Fig. 7c-3).

Figure 8 shows the quantitative assessment of *Phaeodactylum tricorutum* colonized on the surfaces of the samples. There is no significant difference in algal adhesion on all the surfaces after 1 day incubation. After 3 days incubation, the algal adhesion ratio of $\sim 20\%$ for the 316L SS, but only $\sim 17\%$ and $\sim 12\%$ for the as-sprayed coatings and the annealed coatings was observed, respectively. Furthermore, after 7 days incubation, the algal adhesion ratio increases to $\sim 31\%$ on the surface of the 316L SS. However, the adhesion ratio decreases to $\sim 12\%$ and $\sim 1\%$ for the as-sprayed coatings and the annealed coatings, respectively. It is interesting to note that the amount of adhered *Phaeodactylum tricorutum* significantly decreased on the surface of the as-sprayed coatings and especially the annealed coatings. It is likely that corrosion products would affect growth or adhesion of algae,

in turn resulting in constrained adhesion. Consistent with this, it has been reported that heavy metals could bring about damage to DNA by interacting with DNA directly or its replication (Ref 33), and the effect of Cr ions is similar to that of Cu and Hg for photosynthesis and growth of diatoms (Ref 34). It is also likely that as a result of high corrosion rate of the coatings, peeling off of *Phaeodactylum tricorutum* with the corrosion products happened during the incubation.

Conclusions

In this study, Fe-based amorphous/nanocrystalline coatings consisting of $\text{Fe}_{53}\text{Cr}_{19}\text{Zr}_7\text{Mo}_2\text{C}_{18}\text{Si}$ were fabricated by HVOF. The as-sprayed coatings showed remarkably enhanced corrosion resistance as compared to the annealed coatings tested in 3.5 wt.% NaCl solution. It was realized that the as-sprayed coatings with amorphous and nanocrystalline hybrid structures inhibited the attachment of alga, while the annealed coatings showed further enhanced capability of inhibiting the adhesion of algal. This study might open a new window for modifying amorphous coatings for potential marine applications.

Acknowledgments This work was supported by CAS-Iranian Vice Presidency for Science and Technology Joint Research Project (Grant # 174433KYSB20160085), National Natural Science Foundation of China (Grant # 41706076), Qinghai Provincial Innovation Platform Program (No. 2017-ZJ-Y17) and Key Research and Development Program of Zhejiang Province (Grant # 2017C01003).

References

1. M. Lejars, A. Margailan, and C. Bressy, Fouling Release Coatings: A Nontoxic Alternative to Biocidal Antifouling Coatings, *Chem. Rev.*, 2012, **112**(8), p 4347-4390
2. C.G. Soares, Y. Garbatov, A. Zayed, and G. Wang, Influence of Environmental Factors on Corrosion of Ship Structures in Marine Atmosphere, *Corros. Sci.*, 2009, **51**(9), p 2014-2026
3. W. Guo, Y. Wu, J. Zhang, S. Hong, G. Li, G. Ying, J. Guo, and Y. Qin, Fabrication and Characterization of Thermal-Sprayed Fe-Based Amorphous/Nanocrystalline Composite Coatings: An Overview, *J. Therm. Spray Technol.*, 2014, **23**(7), p 1157-1180
4. L. Shan, Y.R. Zhang, Y.X. Wang, J.L. Li, X. Jiang, and J.M. Chen, Corrosion and Wear Behaviors of PVD CrN and CrSiN Coatings in Seawater, *T. Nonferr. Metal. Soc.*, 2016, **26**(1), p 175-184
5. A. Venault, Y. Chang, H.H. Hsu, J.F. Jhong, H.S. Yang, T.C. Wei, K.L. Tung, A. Higuchi, and J. Huang, Biofouling-Resistance Control of Expanded Poly(tetrafluoroethylene) Membrane via Atmospheric Plasma-Induced Surface PEGylation, *J. Membr. Sci.*, 2013, **439**, p 48-57
6. R. Dineshran, R. Subasri, K.R. Somaraju, K. Jayaraj, L. Veda-prakash, K. Ratnam, S.V. Joshi, and R. Venkatesan, Biofouling Studies on Nanoparticle-Based Metal Oxide Coatings on Glass Coupons Exposed to Marine Environment, *Colloid. Surface B*, 2009, **74**(1), p 75-83

7. S.M. Olsen, L.T. Pedersen, M.H. Laursen, S. Kiil, and K. Dam-Johansen, Enzyme-Based Antifouling Coatings: A Review, *Biofouling*, 2007, **23**(5-6), p 369-383
8. A. Daniel, C. Le Pen, C. Archambeau, and F. Reniers, Use of a PECVD-PVD Process for the Deposition of Copper Containing Organosilicon Thin Films on Steel, *Appl. Surf. Sci.*, 2009, **256**(3), p 82-85
9. X. Chen, X. He, X. Suo, J. Huang, Y. Gong, Y. Liu, and H. Li, Effect of Surface Topological Structure and Chemical Modification of Flame Sprayed Aluminum Coatings on the Colonization of *Cylindrotheca Closterium* on Their Surfaces, *Appl. Surf. Sci.*, 2016, **388**, p 385-391
10. Z. Jia, Y. Liu, Y. Wang, Y. Gong, P. Jin, X. Suo, and H. Li, Flame Spray Fabrication of Polyethylene-Cu Composite Coatings with Enwrapped Structures: A New Route for Constructing Antifouling Layers, *Surf. Coat. Technol.*, 2017, **309**, p 872-879
11. D. Li, X. Chen, X. Hui, J. Wang, P. Jin, and H. Li, Effect of Amorphicity of HVOF Sprayed Fe-Based Coatings on Their Corrosion Performances and Contacting Osteoblast Behavior, *Surf. Coat. Technol.*, 2017, **310**, p 207-213
12. H.R. Ma, X.Y. Chen, J.W. Li, C.T. Chang, G. Wang, H. Li, X.M. Wang, and R.W. Li, Fe-Based Amorphous Coating with High Corrosion and Wear Resistance, *Surf. Eng.*, 2016, **33**(1), p 56-62
13. R.J.K. Wood and A.J. Speyer, Erosion-Corrosion of Candidate HVOF Aluminum-Based Marine Coatings, *Wear*, 2004, **256**(5), p 545-556
14. X. Chen, Y. Gong, X. Suo, J. Huang, Y. Liu, and H. Li, Construction of Mechanically Durable Superhydrophobic Surfaces by Thermal Spray Deposition and Further Surface Modification, *Appl. Surf. Sci.*, 2015, **356**, p 639-644
15. A. Kobayashi, S. Yano, H. Kimura, and A. Inoue, Fe-Based Metallic Glass Coatings Produced by Smart Plasma Spraying Process, *Mater. Sci. Eng. B*, 2008, **148**(1-3), p 110-113
16. J.H. Kim and M.H. Lee, A Study on Cavitation Erosion and Corrosion Behavior of Al-, Zn-, Cu-, and Fe-Based Coatings Prepared by Arc Spraying, *J. Therm. Spray Technol.*, 2010, **19**(6), p 1224-1230
17. J. Kwon, H. Park, I. Lee, and C. Lee, Effect of Gas Flow Rate on Deposition Behavior of Fe-Based Amorphous Alloys in Vacuum Kinetic Spray Process, *Surf. Coat. Technol.*, 2014, **259**, p 585-593
18. B. Movahedi, M.H. Enayati, and C.C. Wong, Structural and Thermal Behavior of Fe-Cr-Mo-P-B-C-Si Amorphous and Nanocrystalline HVOF Coatings, *J. Therm. Spray Technol.*, 2010, **19**(5), p 1093-1099
19. J. Kawakita, T. Fukushima, S. Kuroda, and T. Kodama, Corrosion Behaviour of HVOF Sprayed SUS316L Stainless Steel in Seawater, *Corros. Sci.*, 2002, **44**, p 2561-2581
20. M.M. Verdian, K. Raeissi, and M. Salehi, Corrosion Performance of HVOF and APS Thermally Sprayed NiTi Intermetallic Coatings in 3.5% NaCl Solution, *Corros. Sci.*, 2010, **52**(3), p 1052-1059
21. J. Farmer, J.S. Choi, C. Saw, J. Haslam, D. Day, P. Hailey, T. Lian, R. Rebak, J. Perepezko, J. Payer, D. Branagan, B. Beard-sley, A. D'amato, and L. Aprigliano, Iron-Based Amorphous Metals: High-Performance Corrosion-Resistant Material Development, *Metall. Mater. Trans. A*, 2009, **40**(6), p 1289-1305
22. A. Inoue and A. Takeuchi, Recent Development and Application Products of Bulk Glassy Alloys, *Acta Mater.*, 2011, **59**(6), p 2243-2267
23. C. Zhang, R.Q. Guo, Y. Yang, Y. Wu, and L. Liu, Influence of the Size of Spraying Powders on the Microstructure and Corrosion Resistance of Fe-Based Amorphous Coating, *Electrochim. Acta*, 2011, **56**(18), p 6380-6388
24. N. Mahata, A. Banerjee, P. Bijalwan, P.K. Rai, S. Sangal, and K. Mondal, Electrochemical Behavior of HVOF-Sprayed Amorphous and Nanocrystalline Fe-Based $Fe_{73.13}Si_{11.12}B_{10.79}Cr_{2.24}C_{2.72}$ Composite Coatings, *J. Mater. Eng. Perform.*, 2017, **26**(11), p 5538-5552
25. J. Landoulsi, K.E. Cooksey, and V. Dupres, Review-Interactions Between Diatoms and Stainless Steel: Focus on Biofouling and Biocorrosion, *Biofouling*, 2011, **27**(10), p 1109-1124
26. X. He, Y. Liu, Y. Gong, C. Zhou, and H. Li, Autoclaving-Induced In-Situ Grown Alumina on Arc-Sprayed Aluminum Coatings: Multiscaled Topography Facilitates Antifouling Performances, *Surf. Coat. Technol.*, 2017, **309**, p 295-300
27. R.Q. Guo, C. Zhang, Q. Chen, Y. Yang, N. Li, and L. Liu, Study of Structure and Corrosion Resistance of Fe-Based Amorphous Coatings Prepared by HVAF and HVOF, *Corros. Sci.*, 2011, **53**(7), p 2351-2356
28. S. Wang, Y. Li, X. Wang, S. Yamaura, and W. Zhang, Glass-Forming Ability, Thermal Properties, and Corrosion Resistance of Fe-Based (Fe, Ni, Mo, Cr)-P-C-B Metallic Glasses, *J. Non Cryst. Solids*, 2017, **476**, p 75-80
29. L. Qiao, Y. Wu, S. Hong, Y. Qin, W. Shi, and G. Li, Corrosion Behavior of HVOF-Sprayed Fe-Based Alloy Coating in Various Solutions, *J. Mater. Eng. Perform.*, 2017, **26**(8), p 3813-3820
30. R. Li, Z. Li, Y. Zhu, and K. Qi, Structure and Corrosion Resistance Properties of Ni-Fe-B-Si-Nb Amorphous Composite Coatings Fabricated by Laser Processing, *J. Alloys Compd.*, 2013, **580**, p 327-331
31. Y. Yang, C. Zhang, Y. Peng, Y. Yu, and L. Liu, Effects of Crystallization on the Corrosion Resistance of Fe-Based Amorphous Coatings, *Corros. Sci.*, 2012, **59**, p p10-p19
32. J. Kawakita and S. Kuroda, Oscillational Corrosion Potential of HastelloyC Coatings Fabricated by GS-HVOF Spraying, *Corros. Sci.*, 2005, **47**(8), p 2053-2062
33. K. Danadevi, R. Rozati, B. Saleha Banu, P. Hanumanth Rao, and P. Grover, DNA Damage in Workers Exposed to Lead Using Comet Assay, *Toxicology*, 2003, **187**(2-3), p 183-193
34. S. Wiemandersen, Effect of Chromium on Photosynthesis and Growth of Diatoms and Green-Algae, *Physiol. Plant.*, 1974, **32**(4), p 308-310